Zinc hexacyanoferrate as cathode material for aqueous copper-ion batteries

Junchao Liu

A thesis submitted in partial fulfillment of the requirements for the degree of

Master of Science

University of Washington

2022

Committee:

Guozhong Cao

Bruce Hinds

Program Authorized to Offer Degree:

Materials Science and Engineering

University of Washington

Abstract

Zinc hexacyanoferrate as cathode material for aqueous copper-ion batteries

Junchao Liu

Chair of the Supervisory Committee:

Guozhong Cao
Department of Materials Science and Engineering

Bruce Hinds
Department of Materials Science and Engineering

Rechargeable aqueous multivalent ion batteries have attracted increasing attention as an alternative energy storage system for Lithium-ion batteries. In this research, zinc hexacyanoferrate (ZnHCF) is demonstrated as a high-performance cathode material for aqueous copper-ion batteries. It is worth noting that ZnHCF displays remarkable cycling performance with capacity of 55.6 mAh g^{-1} and a capacity retention of ~95% after 3000 cycles. Furthermore, ex-situ XRD reveals the essence of copper ion de-/intercalation mechanism and irreversible structure transition of ZnHCF. Prussian blue analogs are a viable solution in copper-ion batteries despite the problem of ZnHCF dissolution in aqueous solutions.

Introduction

The history of human development is the history of energy development, and the recent industrial revolutions are energy revolutions. However, large-scale storage of energy is a relatively recent event [1]. In 1859, Gaston Planté invented the lead–acid battery, the first-ever battery that could be recharged by passing a reverse current through it. The lead-acid cell was the first "secondary" cell, The lead-acid battery is still used today in automobiles and other applications. In 1899, a Swedish scientist invented named Waldemar Jungner the nickel–cadmium battery, a rechargeable battery that has nickel and cadmium electrodes in a potassium hydroxide solution; the first battery to use an alkaline electrolyte. The first models were robust and had significantly better energy density than lead-acid batteries, but were much more expensive nickel–metal hydride batteries (NiMH) for smaller applications appeared on the market in 1989 as a variation of the 1970s nickel–hydrogen battery. NiMH batteries tend to have longer lifespans than NiCd batteries and, since cadmium is toxic, NiMH batteries are less damaging to the environment. The breakthrough that produced the earliest form of the modern Li-ion battery was made by British chemist M. Stanley Whittingham in 1974, who first used titanium disulfide (TiS_2) as a cathode material, which has a layered structure that can take in lithium ions without significant changes to its crystal structure. John B. Goodenough, after testing a range of alternative materials, replaced TiS_2 with lithium cobalt oxide ($LiCoO_2$, or LCO), which has a similar layered structure but offers a higher voltage and is much more stable in air. Since then, lithium-ion batteries entered the era of commercialization.

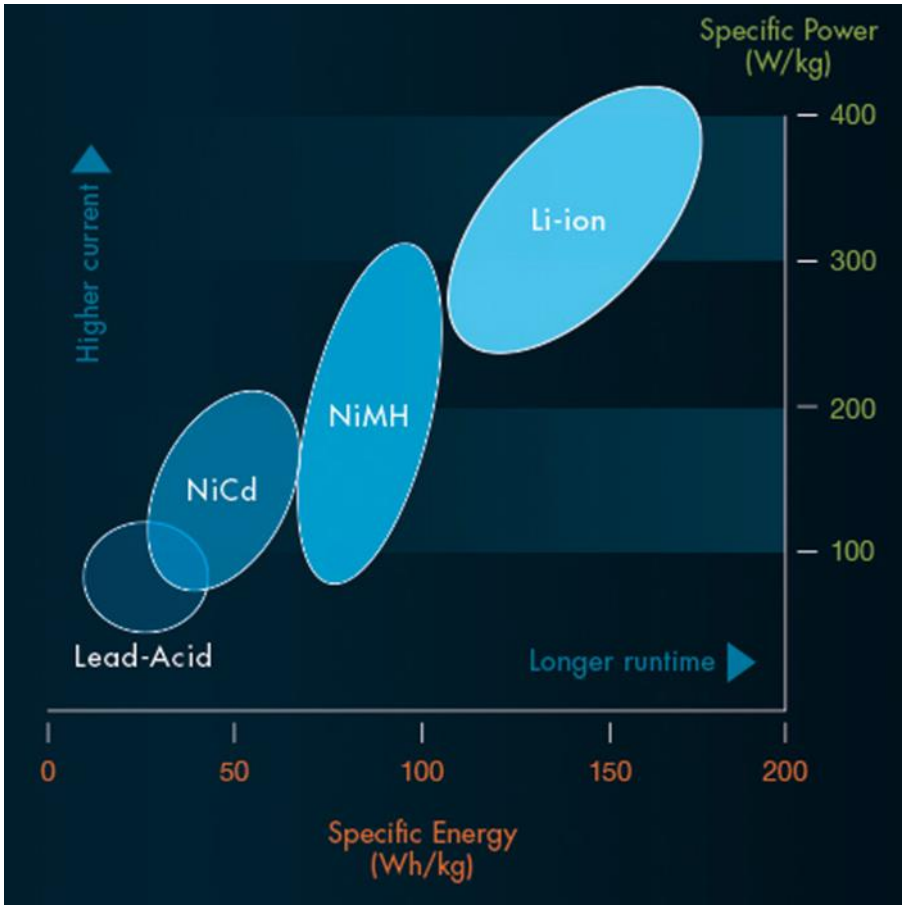

Fig. 1 Specific energy and specific power of rechargeable batteries

Among many battery energy storage technologies, lithium-ion batteries occupy a dominant position because they have the advantages of high energy density, high operating voltage, long cycle life, etc. But safety issues remain a challenge hindering the development of lithium-ion batteries. Lithium-ion batteries that generally use organic electrolytes are prone to fire or explode when they are internally short-circuited. All-solid-state Li batteries with nonflammable solid electrolytes can avoid the safety issues. When compared to liquid-electrolyte Li batteries, all-solid-state ones are believed to be safer, and to have longer cycle life, higher energy density, less requirements on packaging and state-of-charge monitoring circuits. lithium ion-conducting solid electrolytes have been extensively studied, and a number of solid materials, such as, Li_3N [2], LiPON [3], Li_2S-based glass [4], NaSICON-type oxides [5], $Li_{0.05-3x}La_{0.5+x}TiO_3$ [6],

$Li_7La_3Zr_2O_{12}$ [7] and polymer electrolytes [8] have demonstrated fairly good Li-ion conductivity. However, inferior cycle performance induced by the continuous development of interfacial resistance layer between cathode and electrolyte materials is one of the major drawbacks that needs to be overcome. “Water-in-salt” electrolytes is another way to solve safety problems. Suo et described an aqueous electrolyte called the “water-in-salt electrolyte” (WiSE) that contained the currently known water-stable salt LiTFSI at a concentration of 21 M, the $TFSI^-$ anion was implicated in the formation of an SEI layer on the Mo_6S_8 anode, SEI barrier that significantly retarded direct water–electrode contact and electron tunneling [9]. WiSE provides a stable electrochemical reaction environment for lithium-ion batteries in aqueous electrolytes. Although the introduction of high-concentration electrolytes and “water-in-salt” electrolytes in the lithium-ion batteries improves the safety protection, those aqueous system and their narrow voltage window limit the energy density of single-electron carriers batteries. Multivalent metal-ion aqueous batteries such as Mg^{2+},[10] Al^{3+},[11] Zn^{2+},[12] and Ca^{2+}[13] have emerged as alternatives to lithium batteries not only because of their improved safety but also due to their use of earth-abundant metals and high volumetric energy density. Among those aqueous batteries, zinc-ion batteries (ZIBs) are quickly gaining attention by many research groups in recent year. This is because of the following attractive features: (1) the proper redox potential of zinc (-0.763 V vs. a standard hydrogen electrode [SHE]) compared with other multivalent metals (2) high abundance and environmental friendliness (3) long cycle life can be achieved due to the reversibility of Zn plating/stripping (4) a higher volumetric energy density making ZIBs that are small in size is essential for deployment in miniaturized devices such as epidermal, implantable, and wearable sensors. All the above features mean that

there is great potential for the commercialization of Zn-ion batteries. Copper is next to zinc on the periodic table with a theoretical capacity of 844 mAh g^{-1}, have similar ionic radii and energy densities, but has received little attention. An important reason is that copper metal has a high redox potential (0.34 V vs standard hydrogen electrode (SHE)) compared to other types of metal, this results in a very low open circuits potentials and a small voltage window when copper metal is used as the anode material of the battery (Fig. 2) [14]. Recent studies have suggested that the participation of protons in the electrolyte can improve the reaction kinetics [15]. Other metals such as aluminum and zinc are unstable in an acidic environment, but copper is stable, which provides a lot of room for the development of acidic batteries. Another advantage of copper anode is that it does not produce dendrites due to ballistic deposition, this phenomenon can greatly improve battery safety [16].

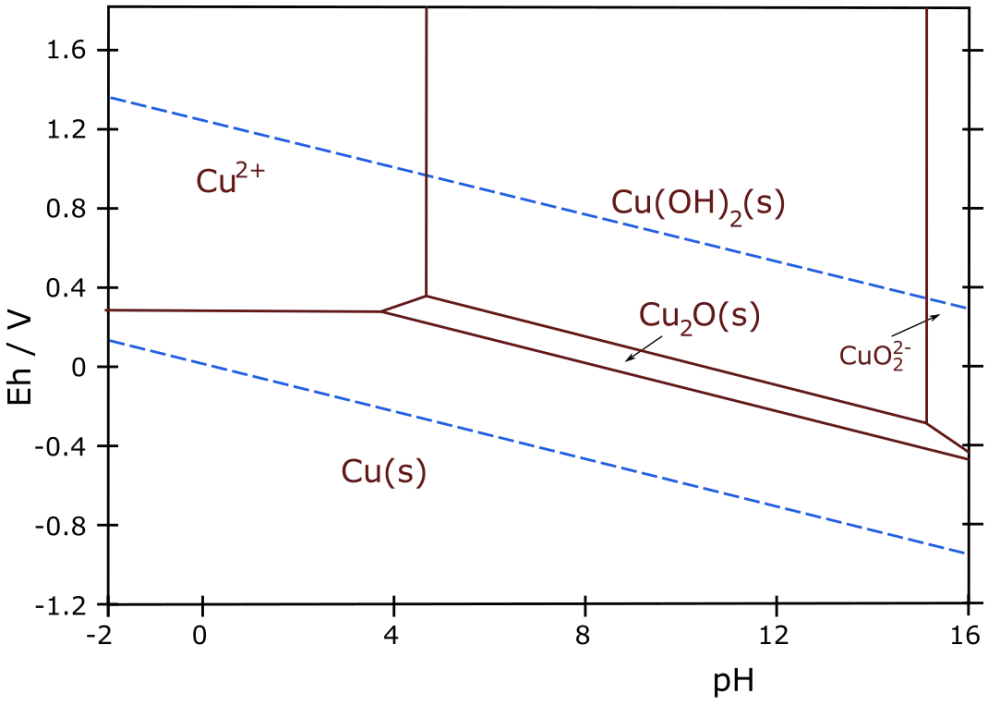

Fig. 2 Pourbaix diagram of the Cu metal

To cooperate with the copper anode to work under acidic conditions and make up for the disadvantage of low open circuit voltage, a cathode material that is stable under acidic conditions with high redox potential must be selected. Among many cathode materials for aqueous batteries, Prussian blue analogues (PBA) are ideal candidate. PBA materials possess the chemical formula of $A_xM[M'(CN)_6]_{1-y}\Upsilon_y \cdot nH_2O$ (where A = alkali metal or alkaline earth metal, M and M' represent the transition metals, Υ is the $[M'(CN)_6]$ vacancies, and $0 \leqslant x \leqslant 2$, $y < 1$), in which the nitrogen-coordinated M cations and carbon-coordinated M' cations in an open framework bridged by cyanide groups (−C≡N−) [Fig. 3][17]. PBA is easy to design and synthesize. When the A, M and M' are multivalent metals, they all become redox-active sites and can provide extra capacity by redox reaction during the charge–discharge processes. Three-dimensional open frameworks of PBA structure provide numerous cavities which allow

reversible intercalation/deintercalation of mobile cations in acidic electrolyte. Also, the relatively high redox potential of the PBA allows the battery to have a higher open circuit voltage to some extent. PBA is widely used in metal-ion batteries such as Zn^{2+} [18], Ca^{2+} [19], Na^{+} [20] and Al^{3+}[21]. However, the cycling stability and the capacity of PBAs is unsatisfactory due to the structural deformation caused by the Jahn–Teller distortion and severe volume change during the ion intercalation/de-intercalation processes [22]. The phenomenon that PBA will dissolve in aqueous solution is also a problem, which may cause instability of the cathode material [23].

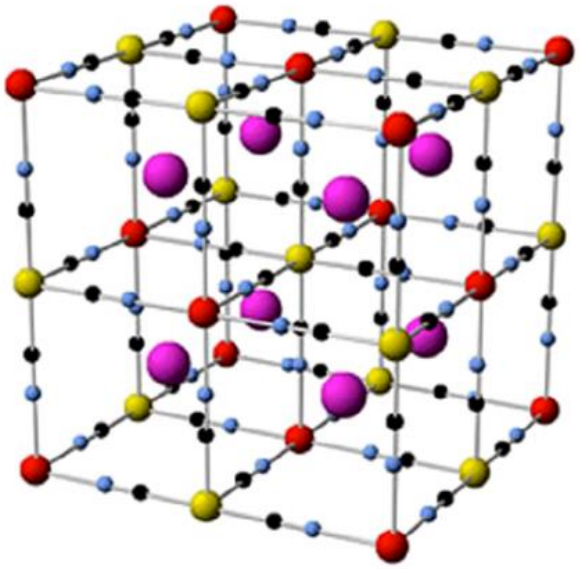

Fig. 3 Prussian Blue structure. Reproduced with permission from [24]

In this work, we synthesized zinc hexacyanoferrates (ZnHCF) compound via a simple hydrothermal method. As a result, the as-obtained ZnHCF as cathode material for aqueous copper-ion battery delivered outstanding performance including high specific capacity (70.1 mAh g^{-1} at 100 mA g^{-1}), ultrahigh rate capability (70% capacity retention at 8000 mA g^{-1}), and stable cycling performance (97% capacity retention over 2800 cycles) due to the high proportion of pseudocapacitive contribution. The intercalation and deintercalation mechanism

of copper ions and its effect on the phase transition of ZnHCF was reveals by ex situ XRD and SEM characterization. Moreover, the dissolution of PBA in electrolyte was discussed. demonstrating the potential of PBA material for future copper-ion battery research.

1. Experimental

Materials synthesis

All chemicals were obtained from Fisher Scientific Inc or Sigma-Aldrich Inc. The zinc hexacyanoferrates (ZnHCF) sample was synthesized using a hydrothermal method. Specifically, a solution of $K_3Fe(CN)_6$ (50 mL, 0.05 M) was gradually added to the $ZnSO_4$ solution (50 mL, 0.1 M) under magnetic stirring. The dropping speeds of solutions were precisely controlled by peristaltic pump. The mixed solution was kept stirring for about 1 hours. After that, the solution was poured into 100 mL Teflon lined stainless steel autoclave and heated up to 120 °C for 6 h. The obtained yellow precipitate was centrifuged, washed with water and ethanol for three times. Then the final sample was dried at 70 °C overnight in an oven.

Material characterizations

X-ray diffraction (XRD) was used to identify the compositions and structures of the products using Bruker D8 Discover X-ray diffractometer with an ImS 2-D detection system (50 kV, 1000 mA). The microstructures of the samples were observed using a scanning electron microscope (Apreo-S LoVac) with an Energy-dispersive X-ray spectrometer (EDS). X-ray photoelectron spectrum (XPS) was taken on a Thermo ESCALAB 250XiX spectrometer with monochromatized Al Kα X-ray (hν ¼ 1486.6 eV). Fourier transform infrared spectroscopy (FTIR) spectra were collected on a Nicolet 6700 spectrometer from 4000 to 400 cm^{-1} using the KBr pellet technique. The metallic contents (K, Zn and Fe) of the PBAs were detected by

inductively coupled plasma-optical emission spectrophotometer (ICP–OES, Perkin Elmer Optima 8300). Thermogravimetric analysis (TA Instruments Q50 thermogravimetric analyzer) was employed to investigate the water content.

Electrochemical measurements

For the preparation of electrodes for electrochemical testing, the active cathode material (FeHCF PBA, 80 wt%) was intimately mixed with carbon black (10 wt%) and polyvinylidene fluoride binder (10 wt%) by hand, using N-methyl-2-pyrrolidone (NMP) as the solvent. Finally, a homogeneous, black slurry was created. The slurry was coated onto a titanium foil current collectors with an area of 0.785 cm^2. The electrodes were dried in the vacuum oven at 80 °C for 12h. Yielded electrode coatings with an active mass loading of approximately 1 mg cm^{-2}. Electrochemical performance was tested using CR2032 coin-type cells fabricated in air. 1 M $CuSO_4$ aqueous solution was used

as the electrolyte. A piece of qualitative filter paper (Qualitative Filter Paper, Grade 610, Ahlstrom) soaked in the electrolyte was used as separator. Copper foil was served as anode. Electrochemical tests were performed on the Neware battery testing system. The redox characteristics of the cathodes were tested by cyclic voltammetry (CV) in a voltage window of 0.2–0.9 V on a Solartron electrochemical station (SI 1287) equipped with an electrochemical impedance spectroscopy system (EIS, SI 1260). Electrochemical impedance spectroscopy (EIS) measurements were performed in the frequency range from 100 kHz to 0.01 Hz.

2. Results and discussion

Zinc hexacyanoferrate (ZnHCF) are prepared by a simple hydrothermal method. X-ray diffraction (XRD) is conducted to investigate the crystal structural information. As the XRD pattern of ZnHCF shown in Fig.1a, the position and intensity of diffractive peaks well match with rhombohedral phase zinc hexacyanoferrate ($Zn_3(Fe(CN)_6)_2$, JCPDS card no. 38-688), which shows that pure ZnHCF is obtained. Fourier transform infrared (FTIR) is used to analyze the coordination condition of chemical bonds in ZnHCF. As revealed by the FTIR spectra, the band at 2092 cm^{-1} corresponds to the C≡N stretching vibration in Fe^{II}–C≡N–Zn^{II}. Peaks at 2135 cm^{-1} was assigned to the Fe^{II}-C≡N-Fe^{III} chain, this shows that a certain amount of Fe originally connected to C was rearranged during the synthesis process and reconnected to N [25]. Peaks at 2162 and 2185 cm^{-1} refer to the C≡N stretching in Fe^{III}–C≡N–Zn^{II} of the cubic and rhombohedral phases, respectively (Fig. 4b) [26]. Although the peak of cubic phase does not appear in XRD pattern, this indicates that there is a small amount of ZnHCF in cubic phase. X-ray photoelectron spectroscopy (XPS) is conducted to determine the elementary valence state of ZnHCF (Fig. 4c). In The Fe 2p region, the Fe 2p3/2 and Fe 2p1/2 peaks at 708.6 eV and 721.6 eV, respectively, with 13.0 eV spin energy separation could be attributed to the presence of Fe^{II}, and two binding energies with peaks located at 713.3 eV and 725.7 eV indicated the oxidation state of Fe^{III}. The XPS pattern further proves that atomic rearrangement occurs during the synthesis of ZnHCF, because the transition metal attached to N exhibits high spin characteristics. The K, Zn, and Fe contents of the ZnHCF are investigated by inductively coupled plasma optical emission spectrometer (ICP–OES). As the results are shown in Table S1, the K/Zn/Fe molar ratio of ZnHCF is 0.14:1.6:1, which is very close to the Zn/Fe ratio of the standard zinc hexacyanoferrate. Water contents are calculated based on the weight loss at

200 °C from thermogravimetric analysis (TGA). Below 200 degrees is the removal of crystal and absorbed water, which indicates the existence of 1.35 H_2O per ZnHCF unit (Fig.4d). Combining above results, the chemical formula is found to be $K_{0.14}Zn_{1.6}Fe_x[Fe_{1-x}(CN)_6]\cdot 1.35H_2O$. Based on Faraday's law, the theoretical capacity of ZnHCF can be calculated as 77.4 mAh g^{-1}, details shown in supporting information note S1. The scanning electron microscopy (SEM) exhibits octahedron morphology of ZnHCF with some irregular crystal attachment and the size distribution within a narrow range of 3–5 μm (Fig. 4e). An image with clearer details is shown in Figure S2. The element mapping results display that the elements K, Zn and Fe were homogeneously distributed in the ZnHCF.

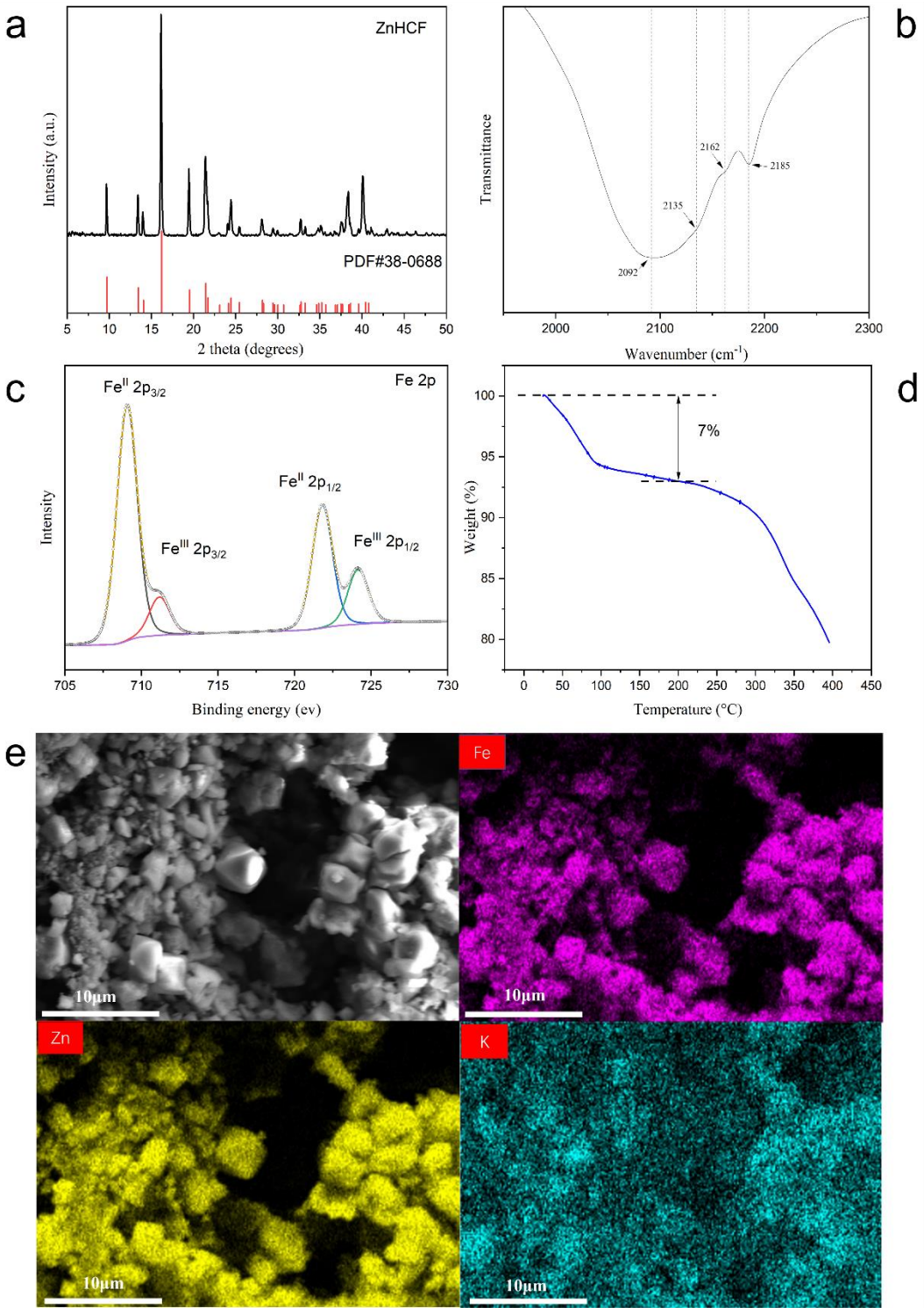

Fig.4 a) The XRD pattern of ZnHCF. b) FTIR spectrum c) The fitting XPS spectrum of Fe 2p region. d) TG curve of ZnHCF from room temperature to 200 °C at a heating rate of 5 °C/min. e) The SEM image of ZnHCF and EDS mapping of Fe, Zn, K elements.

Cyclic voltammetry (CV) is conducted to assess the electrochemical properties. CV curves were collected at 0.1 mV s^{-1} in the voltage range of 0.2–0.9 V for three cycles (Fig. 5a). It can be seen that the ZnHCF cathode exhibits two pairs of redox peaks. The potential difference within each redox pair is very small, which indicating a highly reversible electrochemical reaction. The pair of peaks around 0.5 V/0.57 V belong to the Fe^{II}/Fe^{III} redox couples, in which the Fe with a high-spin configuration coordinated to nitrogen. Another pair of peaks around 0.77 V/0.85 V also belongs to the Fe^{II}/Fe^{III} redox couples, but the Fe in it is coordinated to carbon with a low-spin configuration. The redox potential of low-spin Fe in ZnHCF is higher than that of high-spin Fe due to the higher ligand field stabilization energy (LFSE) of LS-Fe since carbon is a higher field ligand compared with nitrogen [27]. The peak current density of the redox couple in the first circle is very large, and it can be said that there are many Fe^{II} converted to Fe^{III}. which is consistent with the presence of a large amount of Fe^{II} in pristine ZnHCF.

CV curves at various scan rates were measured to further investigate the electrochemical kinetics. As the scan rate increases, the CV curves retain their original shape, but the voltage gaps of redox peaks increase due to polarization (Fig. 5b). The following empirical equation of the peak current i and the scan rate v is employed to analyze the dominant factor governing the electrochemical process [28]:

$$i = av^b, \quad (1)$$

in which parameter a and b are adjustable parameters. The b value of 1 corresponds to a surface-controlled process, while b = 0.5 is indicative of a diffusion-controlled process. b values were calculated, shown in Fig. 3c. The b values of peaks a–d in ZnHCF are in the range of 0.5 to 1

and close to 1, which suggests that the predominant surface controlled process in both redox reactions. The current at a fixed voltage of a certain scan rate (v) can be divided into capacitive (k_1v) and diffusion-controlled ($k_2v^{1/2}$) contributions based on the equation:

$$i = k_1 v + k_2 v^{1/2} \quad (2)$$

where coefficients k_1 and k_2 can be quantitatively calculated through the fitting of $i/v^{1/2}$ vs. $v^{1/2}$ plots according to the variant of Equation (2):

$$i/v^{1/2} = k_1 v^{1/2} + k_2 \quad (3)$$

Based on this equation (3), the capacitance contribution rate at various scan rates is calculated. In ZnHCF, an 85.5% fraction of the capacity is assigned to the capacitive contribution at a scan rate of 0.1 mV s^{-1}, and the capacitive contribution gradually increases to 94.7% at a scan rate of 1.2 mV s^{-1}, this characteristic is advantageous to attain quicker ion diffusion at high scan rates or high current densities (Fig. 5d). Electrochemical impedance spectroscopy (EIS) is conducted to evaluate the impedance of electron transfer and copper ions diffusion. The Nyquist plots of EIS data of ZnHCF shown in Fig. 5e. The charge transfer resistance (R_{ct}) represented by the semicircle in the high frequency region. ZnHCF presents a R_{ct} of 63 Ω in the initial state and the charge transfer resistances increases to 80 Ω after 15 times CV cycles. It is possible that substances formed during the reaction hinder electron transport. The linear part at low frequencies can be used to evaluate ion diffusion coefficients ($D_{Cu^{2+}}$) based on slope values of Z' -$\omega^{-1/2}$ (Fig. 5f). In the equation R, T, A, n, F, C and σ_w denote the gas constant, absolute temperature, surface area of electrode, charge-transfer number, Faraday constant, Cu^{2+} concentration and Warburg factor, respectively [29].

$$D_{Cu^{2+}}^{EIS} = \frac{R^2T^2}{2A^2n^4F^4C^2\sigma_w^2}$$

Before the CV cycling, the diffusion coefficient of ZnHCF is 7.88×10^{-13} cm^2 s^{-1}. After 15 times of CV cycles, the diffusion coefficient of ZnHCF increase to 5.19×10^{-12} cm^2 s^{-1}. This phenomenon may be due to the gradual wetting of the electrodes and the electro-activation process caused by the trapped Cu^{2+}, and can also explain rising capacities at the beginning of the cycling process, which will be described in the following section [30].

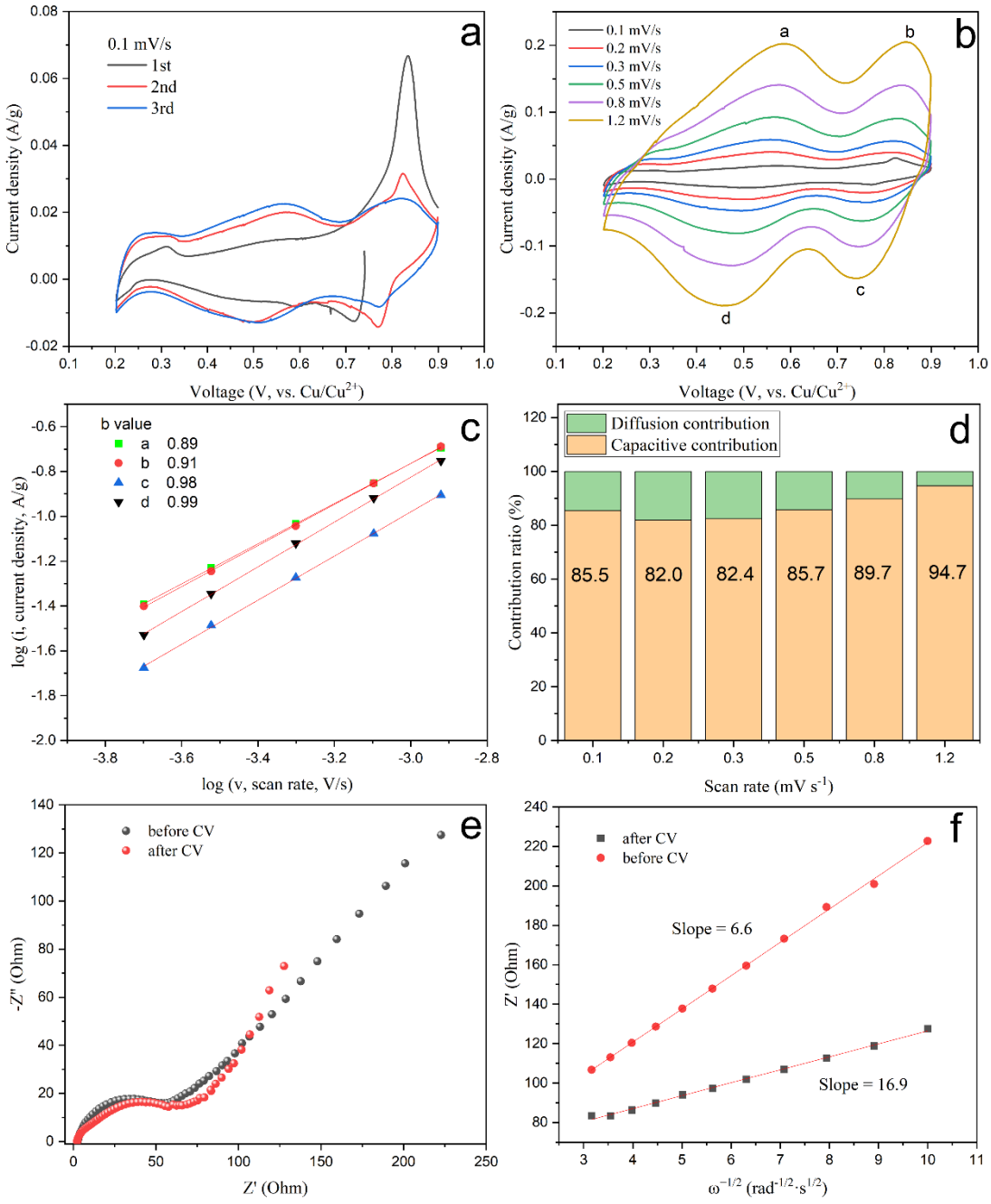

Fig. 5 a) CV curves of ZnHCF collected at a scan rate of 0.1 mV s^{-1}. b) The CV curves measured at scan rates of 0.1–1.2 mV/s. c) the relationship between peak currents and scan rates. d) Capacitive contribution ratio of capacitive and diffusion-controlled capacities at different scan rates. e) EIS patterns of ZnHCF before and after 15 cycles of cv test. f) The relationship between Z' and $\omega^{-1/2}$ at low frequency.

The galvanostatic charge/discharge profiles for ZnHCF within the cutoff potentials of 0.2–0.8 V vs. Cu/Cu^{2+} at a current density of 100mAh g^{-1} are shown in Fig. 6a. ZnHCF cathode can deliver a discharge capacity of 65.4 mAh g^{-1} in the first cycle. However, during charging process, the voltage is difficult to reach 0.9 V. Corresponding to the CV pattern, between 0.8 V and 0.9 V is the chemical reaction of Fe^{II} into Fe^{III}, oxidation products will dissociate [31]. After setting the upper voltage limit to 0.8 V, the coulombic efficiency reaches more than 80%. After 10 cycles, 20 cycles of charging and discharging, the discharge capacity is basically unchanged, but the Coulombic efficiency gradually decreases. Fig. S2 is the charge-discharge range from 0.2V to 0.9 V, it can be seen from the figure that the Coulomb efficiency is only 20%. In the tenth cycle, the voltage cannot be charged to 0.9 V. Fig. 6b reports the corresponding rate performance of samples at various current densities. ZnHCF exhibits an excellent capacities of 65, 63, 57, 52 and 45 mAh g^{-1} at 0.5, 1, 2, 4 and 8 A g^{-1}, respectively. Reversible capacity of 73 mAh g^{-1} can be maintained when the rate returns to 0.5 A g^{-1}, indicating a good structure stability and the high electrochemical reversibility of ZnHCF at high rates. Cycling stability are shown in Fig. 6c at a higher discharge current density (2 A g^{-1}), the Capacity of ZnHCF cathode increases over the first 150 cycles and retained on 48 mA h g^{-1}. ZnHCF demonstrates a capacity retention of 97% over 2850 cycles (Compared with the first circle after activation), uncovering outstanding capacity stability. Unlike cycling under low currents, coulombic efficiency can be maintained above 95% under high current. Fig. S3 are the SEM images of ZnHCF before and after 3000 charge/discharge cycles at 2 A g^{-1}. The general morphology has basically not experienced serious degradation, which is consistent with the excellent long-term cycle stability. But the bulk ZnHCF has gradually broken down into

smaller pieces, the original smooth surface is now become loose and rough. Table S2 shows that ZnHCF is used in other metal-ion batteries, the performance is better when used in copper ion batteries.

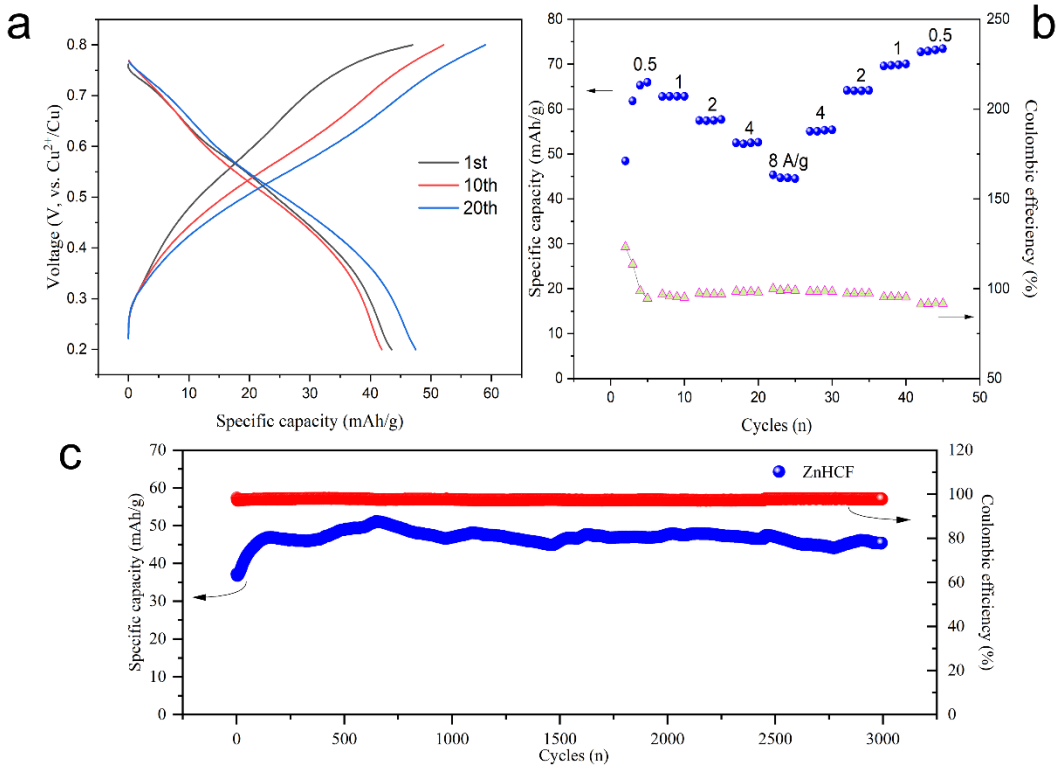

Fig. 6 (a) Voltage profiles of ZnHCF at 100 mA g-1. (b) Rate capability and (c) Cycling stability in the aqueous Copper-ion battery.

The ex-situ XRD was carried out to study the copper storage mechanism and structural evolution of ZnHCF cathode at different discharge-charge states. In Fig. 7, the pattern from bottom to top is discharge from pristine state (0.75V) to 0.2V and charge to 0.9V. The strong peak of the pristine state around 16.2° in Fig. 7a, 19.5° in Fig. 7b, 21.4°, and 21.7° in Fig. 7c well match (113), (024), (116), and (211) planes of rhombohedral phase zinc hexacyanoferrate (JCPDS card no. 38-688). When the pristine electrode was discharged to 0.2 V, the intensity of (113) and (024) peaks decrease, and the position slightly move to a higher angle. This is due to

the intercalation of copper ions and the formation of $[Fe^{II}(CN)_6]^{4-}$ [32]. During charge process, these two peaks gradually recover to the original state. (116) and (211) peaks are gradually separated during discharging, the former moves to a higher angle, and the intensity of the latter is decreased. During charging, the pattern evolves in a reverse way comparing with that in the discharging process except that the intensity of (211) peak is finally greater than that of (116) peak. At the position of 17.6° in Fig. 7a, a peak appears, and the peak intensity is getting stronger, and it does not disappear in the fully charged state. This peak corresponds to the characteristic of the (200) peak of the cubic phase hexacyanoferrate (JCPDS card no. 38-687). The position of this peak appears to the right of the (200) peak in the standard card, which also conforms to the above-mentioned characteristics of several peaks moving to a higher angle during the copper ions intercalation. In Fig. S4, after 3000 cycles of charge and discharge, the characteristic peaks of the rhombohedral phase disappeared completely and were replaced by the characteristic peaks of the cubic phase. These illustrate that the ZnHCF undergoes an irreversible rhombohedral–cubic phase transition during the copper-ion intercalation/de-intercalation process in aqueous environment.

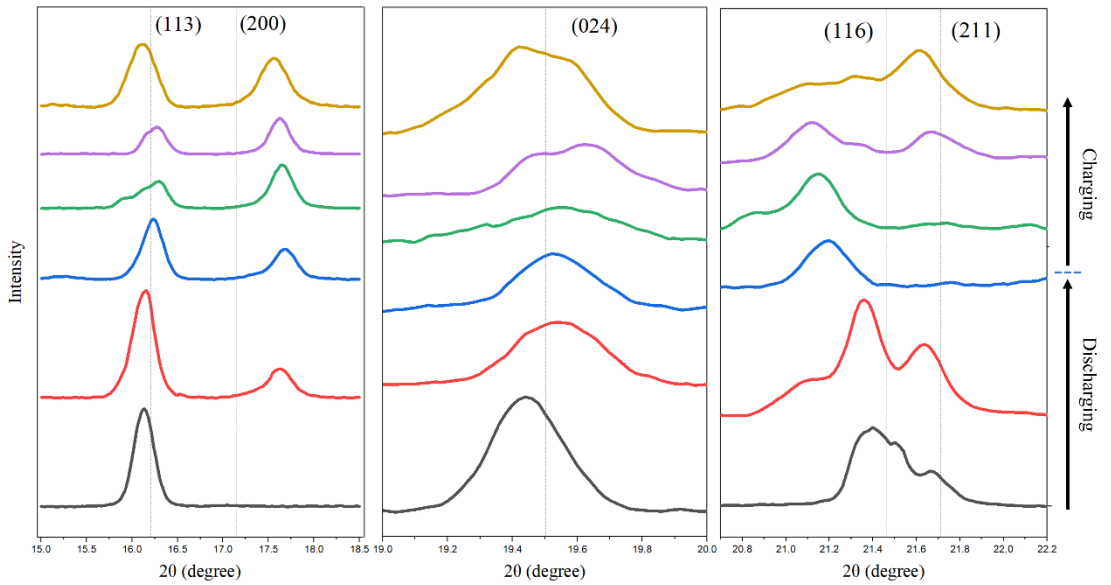

Fig. 7 ex-situ XRD patterns of ZnHCF collected at different charge/discharge states

Not only electrochemical reactions can cause this phase transition, but simple immersion into aqueous solutions can also cause this transition. Cubic ZnHCF is more soluble than the rhombohedral phase [33]. So, when this transition occurs, there is an irreversible loss of voltage and capacity. It can be seen from Fig. S5a that when a pure $CuSO_4$ electrolyte is used, the open circuit voltage dropped to 0.2 V in only 125 minutes. When the concentration of copper ion is increasing, the voltage drop is faster, indicating that copper ion will accelerate the dissolution. The SEM image illustrates that the surface of the copper anode will be covered with a layer of ZnHCF (Fig. 8b) compare with the smooth surface of the copper anode (Fig. 8a), which makes the reaction of the copper anode more difficult, which brings great problems to the normal use of the battery. Preventing the dissolution of the cathode material and its migration to the anode is an important part of improving battery stability. Following part is assembling half-cells with different types of separators and concentrations of electrolytes to investigate inhibition of cathode material dissolution and migration.

Fig. S5b shows the standing time versus open circuit voltage curves of coin cells using different separators. The cell with glass fiber has the fastest voltage drop, AHL second, and polypropylene (PP) the slowest. SEM images showing the morphology of different separator materials (Fig. S6). Glass fiber separator consists of randomly arranged fibers, which create a network structure. For the AHL filter paper, it has evenly distributed micropores with a diameter of 1.5 μm. Pores with 0.45 μm size are uniformly distributed in the PP separator. Fig. 5c shows the surface of the copper anode for the cell with the separator cycled for 3000 cycles. The surface of the copper anode is covered with many ZnHCF. When using an AHL filter as a separator, fewer ZnHCF cover the copper anode, the phenomenon of migration is greatly reduced (Fig. 8d). It can also be seen from the figure that, unlike lithium-ion batteries and zinc-ion batteries, there is no dendrite formation on the surface of the anode of copper ion batteries. A scaly morphology surface is obtained after long-term cycling. This phenomenon can be related to the kinetic roughening process with ballistic deposition [34]. This feature of copper ion battery can greatly improve the safety of the battery. These results indicate that the reduction of pore size can effectively prevent migration. It has been reported that solutions with zinc ions can prevent the dissolution of ZnHCF [31]. As illustrated in Fig. S5c, in many electrolytes with different concentrations of $ZnSO_4$ added, the voltage of 1M $CuSO_4$+1M $ZnSO_4$ decreases the slowest. When using 1M $CuSO_4$+1M $ZnSO_4$ as the electrolyte, the CV curve is basically the same as using 1M $CuSO_4$ (Fig. S6a). Within the cutoff potentials of 0.2–0.9 V vs. Cu/Cu^{2+} at a current density of 50 mAh g^{-1}, Coulombic efficiency increased to 50% (Fig. S6c). Under the long-term cycling performances, ZnHCF delivered a capacity of 60 mAh g^{-1} with 95% capacity

retention over 3000 cycles at 2A g^{-1}, which shows that adding zinc ions to the electrolyte can improve the electrochemical performance (Fig. S6d).

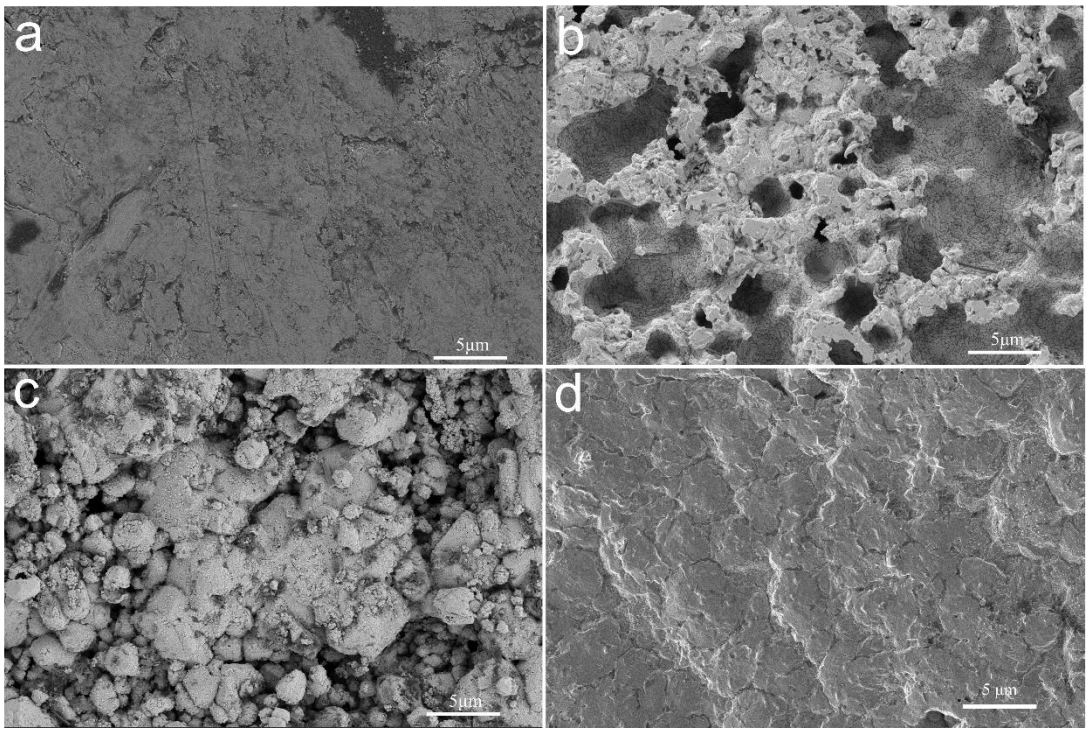

Fig. 8 SEM images of copper anode (a) pristine state (b) Stand for 24h with 1M CuSO4 electrolyte and glassfiber separator (c) after 3000 cycles of charge/discharge with 1M $CuSO_4$ electrolyte and glassfiber separator (d) after 3000 cycles of charge/discharge with 1M $CuSO_4$ electrolyte and AHL separator

3. Conclusion

In brief, we construct an aqueous rechargeable copper-ion battery based on ZnHCF as cathode material. The ZnHCF demonstrates an excellent capacity retention of 96% over

2850 cycles at high current density (2 A g^{-1}) and outstanding rate performance and reversibility. CV curves show capacitive contribution-dominated electrochemical processes, demonstrating superior reaction kinetics for copper-ion batteries. Besides, ex-situ XRD and SEM results reveal de-/intercalation mechanism of copper ions and ZnHCF retains morphological stability but

undergoes an irreversible cubic phase transition during battery cycling. The problem that ZnHCF is easy to dissolve in aqueous solution has also been explored. After the application of the new electrolyte and separator, the dissolution problem has been alleviated, and the capacity and Coulombic efficiency have been improved. Our work explores a new direction for the research of higher performance copper-ion batteries.

4. Future work

The future research direction can be to find a Prussian Blue Analog or a high-redox-potential material that is stable in aqueous solution as a cathode material. Increasing the concentration of protons is also a research direction, and exploring the co-intercalation mechanism of protons and copper ions can regulate the reaction kinetics. It is also important to explore the inhibition of ZnHCF dissolution by the type of electrolyte or the inhibition of migration by the separator.

Acknowledgements

First of all, I would like to thank my parents for their material and spiritual support, so that I can concentrate on studying and researching in a foreign country without distractions. Secondly, I would like to thank University of Washington for giving me such a beautiful environment. From the Quad to the Drumheller Fountain, everywhere tells the rich historical heritage of this century-old school. I would also like to thank Professor Guozhong Cao and every member of the Cao Lab. Without your help and guidance, it is difficult for me to make great progress in scientific research. Finally, I would like to thank the research platform and patient and experienced instructors provided by the School of Engineering, which have provided almost all help to my scientific research.

Reference

[1] Wikipedia contributors. "History of the battery." Wikipedia, The Free Encyclopedia. Wikipedia, The Free Encyclopedia, 15 Jul. 2022. Web. 2 Aug. 2022.

[2] Kızılaslan, A., & Akbulut, H. (2019). Assembling All‐Solid‐State Lithium‐Sulfur Batteries with Li3N‐Protected Anodes. ChemPlusChem, 84(2), 183-189.

[3] Sepúlveda, A., Criscuolo, F., Put, B., & Vereecken, P. M. (2019). Effect of high temperature LiPON electrolyte in all solid state batteries. Solid State Ionics, 337, 24-32.

[4] Hakari, T., Hayashi, A., & Tatsumisago, M. (2017). Li2S‐Based Solid Solutions as Positive Electrodes with Full Utilization and Superlong Cycle Life in All‐Solid‐State Li/S Batteries. Advanced Sustainable Systems, 1(6), 1700017.

[5] Harada, M., Takeda, H., Suzuki, S., Nakano, K., Tanibata, N., Nakayama, M., ... & Takeuchi, I. (2020). Bayesian-optimization-guided experimental search of NASICON-type solid electrolytes for all-solid-state Li-ion batteries. Journal of Materials Chemistry A, 8(30), 15103-15109.

[6] Zhou, W., Li, Y., Xin, S., & Goodenough, J. B. (2017). Rechargeable sodium all-solid-state battery. ACS central science, 3(1), 52-57.

[7] Kotobuki, M., Munakata, H., Kanamura, K., Sato, Y., & Yoshida, T. (2010). Compatibility of Li7La3Zr2O12 solid electrolyte to all-solid-state battery using Li metal anode. Journal of the Electrochemical Society, 157(10), A1076.

[8] Agrawal, R. C., & Pandey, G. P. (2008). Solid polymer electrolytes: materials designing and all-solid-state battery applications: an overview. Journal of Physics D: Applied Physics, 41(22), 223001.

[9] Suo, L., Borodin, O., Gao, T., Olguin, M., Ho, J., Fan, X., ... & Xu, K. (2015). "Water-in-salt" electrolyte enables high-voltage aqueous lithium-ion chemistries. Science, 350(6263), 938-943.

[10] Canepa, P., Sai Gautam, G., Hannah, D. C., Malik, R., Liu, M., Gallagher, K. G., ... & Ceder, G. (2017). Odyssey of multivalent cathode materials: open questions and future challenges. Chemical reviews, 117(5), 4287-4341.

[11] Muldoon, J., Bucur, C. B., & Gregory, T. (2014). Quest for nonaqueous multivalent secondary batteries: magnesium and beyond. Chemical reviews, 114(23), 11683-11720.

[12] Song, M., Tan, H., Chao, D., & Fan, H. J. (2018). Recent advances in Zn‐ion batteries. Advanced Functional Materials, 28(41), 1802564.

[13] Gummow, R. J., Vamvounis, G., Kannan, M. B., & He, Y. (2018). Calcium‐ion batteries: current state‐of‐the‐art and future perspectives. Advanced Materials, 30(39), 1801702.

[14] Bard, A. J., Parsons, R., & Jordan, J. (2017). Nitrogen, phosphorus, arsenic, antimony, and bismuth. In Standard Potentials in Aqueous Solution (pp. 127-188). Routledge.

[15] Liu, W., Dong, L., Jiang, B., Huang, Y., Wang, X., Xu, C., ... & Kang, F. (2019). Layered vanadium oxides with proton and zinc ion insertion for zinc ion batteries. Electrochimica Acta, 320, 134565.

[16] Lafouresse, M. C., Heard, P. J., & Schwarzacher, W. (2007). Anomalous scaling for thick electrodeposited films. Physical review letters, 98(23), 236101.

[17] Yi, H., Qin, R., Ding, S., Wang, Y., Li, S., Zhao, Q., & Pan, F. (2021). Structure and properties of prussian blue analogues in energy storage and conversion applications. Advanced Functional Materials, 31(6), 2006970.

[18] Tojo, T., Sugiura, Y., Inada, R., & Sakurai, Y. (2016). Reversible calcium ion batteries using a dehydrated prussian blue analogue cathode. Electrochimica Acta, 207, 22-27.

[19] Zeng, Y., Lu, X. F., Zhang, S. L., Luan, D., Li, S., & Lou, X. W. (2021). Construction of Co–Mn Prussian Blue Analog Hollow Spheres for Efficient Aqueous Zn‐ion Batteries. Angewandte Chemie International Edition, 60(41), 22189-22194.

[20] Zhu, Y., Zhang, Z., Bao, J., Zeng, S., Nie, W., Chen, P., ... & Xu, Y. (2020). Multi‐metal doped high capacity and stable Prussian blue analogue for sodium ion batteries. International Journal of Energy Research, 44(11), 9205-9212.

[21] Ru, Y., Zheng, S., Xue, H., & Pang, H. (2020). Potassium cobalt hexacyanoferrate nanocubic assemblies for high-performance aqueous aluminum ion batteries. Chemical Engineering Journal, 382, 122853.

[22] Gebert, F., Cortie, D. L., Bouwer, J. C., Wang, W., Yan, Z., Dou, S. X., & Chou, S. L. (2021). Epitaxial Nickel Ferrocyanide Stabilizes Jahn‐Teller Distortions of Manganese Ferrocyanide for Sodium‐Ion Batteries. Angewandte Chemie, 133(34), 18667-18674.

[23] Grandjean, F., Samain, L., & Long, G. J. (2016). Characterization and utilization of Prussian blue and its pigments. Dalton transactions, 45(45), 18018-18044.

[24] Bazzicalupi, C., Bianchi, A., García-España, E., & Delgado-Pinar, E. (2014). Metals in supramolecular chemistry. Inorganica Chimica Acta, 417, 3-26.

[25] Gerber, S. J., & Erasmus, E. (2018). Electronic effects of metal hexacyanoferrates:

An XPS and FTIR study. Materials Chemistry and Physics, 203, 73-81.

[26] Rodríguez-Hernández, J., Reguera, E., Lima, E., Balmaseda, J., Martínez-García, R., & Yee-Madeira, H. (2007). An atypical coordination in hexacyanometallates: Structure and properties of hexagonal zinc phases. Journal of Physics and Chemistry of Solids, 68(9), 1630-1642.

[27] Sun, J., Ye, H., Oh, J. A. S., Plewa, A., Sun, Y., Wu, T., ... & Lu, L. (2021). Elevating the discharge plateau of Prussian blue analogs through low-spin Fe redox induced intercalation pseudocapacitance. Energy Storage Materials, 43, 182-189.

[28] Jiang, Y., & Liu, J. (2019). Definitions of pseudocapacitive materials: a brief review. Energy & Environmental Materials, 2(1), 30-37.

[29] Zhang, X., Xia, M., Liu, T., Peng, N., Yu, H., Zheng, R., ... & Shu, J. (2021). Copper hexacyanoferrate as ultra-high rate host for aqueous ammonium ion storage. Chemical Engineering Journal, 421, 127767.

[30] Zheng, J., Liu, C., Tian, M., Jia, X., Jahrman, E. P., Seidler, G. T., ... & Cao, G. (2020). Fast and reversible zinc ion intercalation in Al-ion modified hydrated vanadate. Nano Energy, 70, 104519.

[31] Zhang, J., Huang, H., Bae, J., Chung, S. H., Zhang, W., Manthiram, A., & Yu, G. (2018). Nanostructured host materials for trapping sulfur in rechargeable Li–S batteries: structure design and interfacial chemistry. Small Methods, 2(1), 1700279.

[32] Li, Q., Ma, K., Hong, C., Yang, Z., Qi, C., Yang, G., & Wang, C. (2021). High-voltage K/Zn dual-ion battery with 100,000-cycles life using zero-strain ZnHCF cathode. Energy Storage Materials, 42, 715-722.

[33] Ni, G., Han, B., Li, Q., Ji, Z., Huang, B., & Zhou, C. (2016). Instability of Zinc Hexacyanoferrate Electrode in an Aqueous Environment: Redox-Induced Phase Transition, Compound Dissolution, and Inhibition. ChemElectroChem, 3(5), 798-804.

[34] Lafouresse, M. C., Heard, P. J., & Schwarzacher, W. (2007). Anomalous scaling for thick electrodeposited films. Physical review letters, 98(23), 236101.

Supporting information

Note 1

According to the Faraday's law, Qtheoretical = (nF) / (3600*Mw) mAh g^{-1}, n is the number of charge carrier, F is the Faraday constant and Mw is the molecular weight of the active material used in the electrode. In our case for $K_{0.14}Zn_{1.6}[Fe(CN)_6]\cdot 1.35H_2O$, n is 1, Mw is 346.14 g mol^{-1} and thus the theoretical capacity is 77.4 mAh g^{-1}.

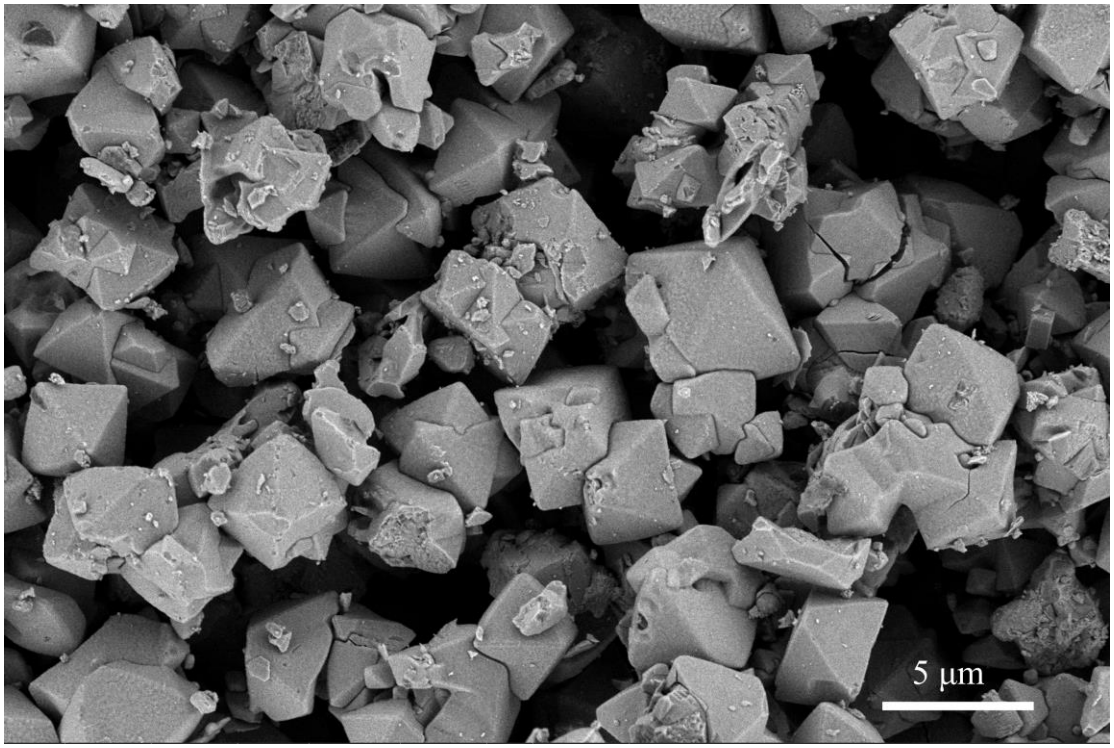

Fig. S1 SEM images of ZnHCF

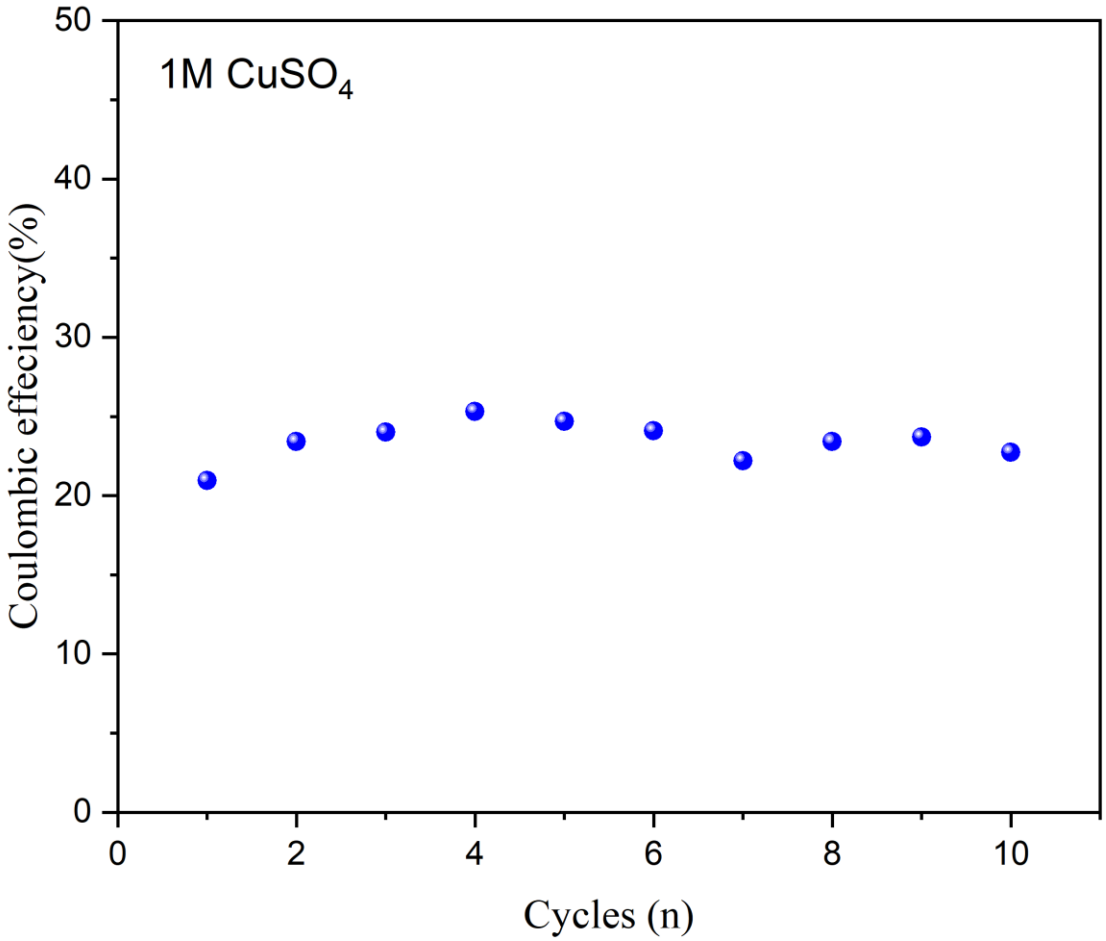

Fig. S2 Coulombic efficiency of charge-discharge ranges from 0.2V to 0.9 V with 1M $CuSO_4$ electrolyte

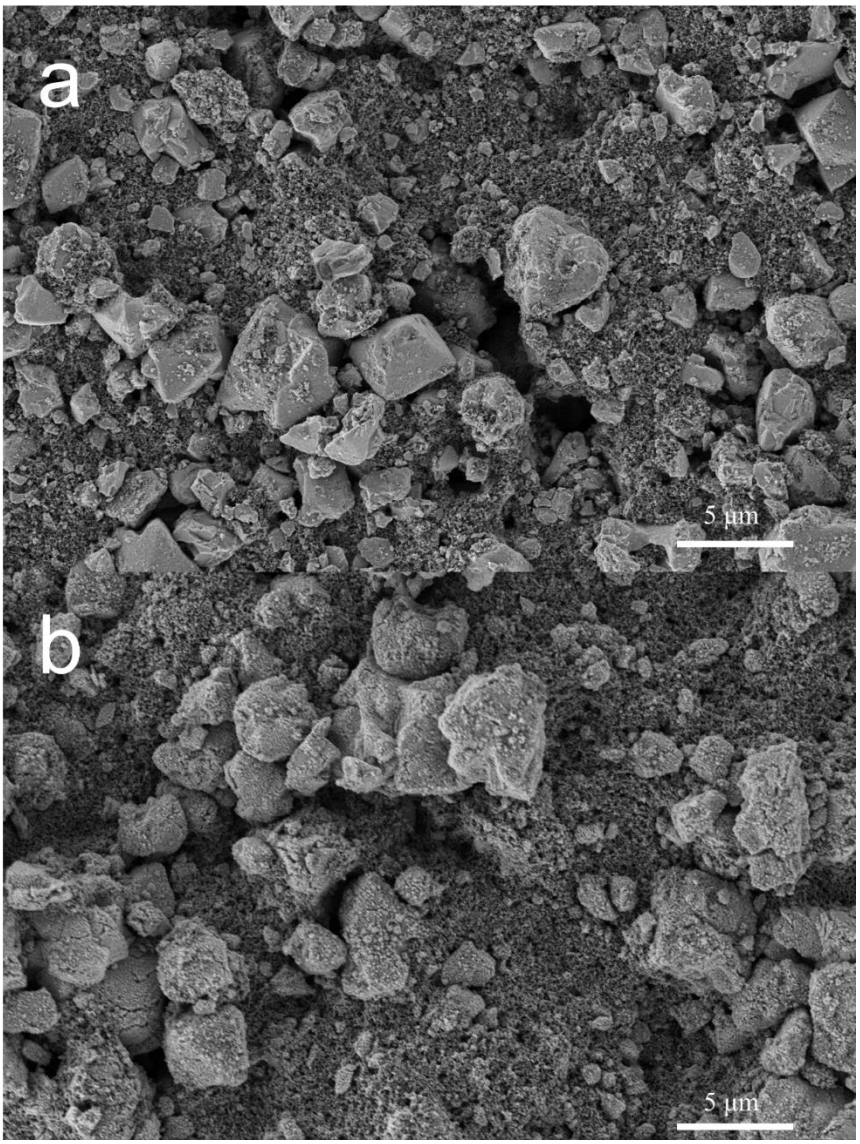

Fig. S3 SEM images of cathode material (a) before and (b) after 3000 cycles

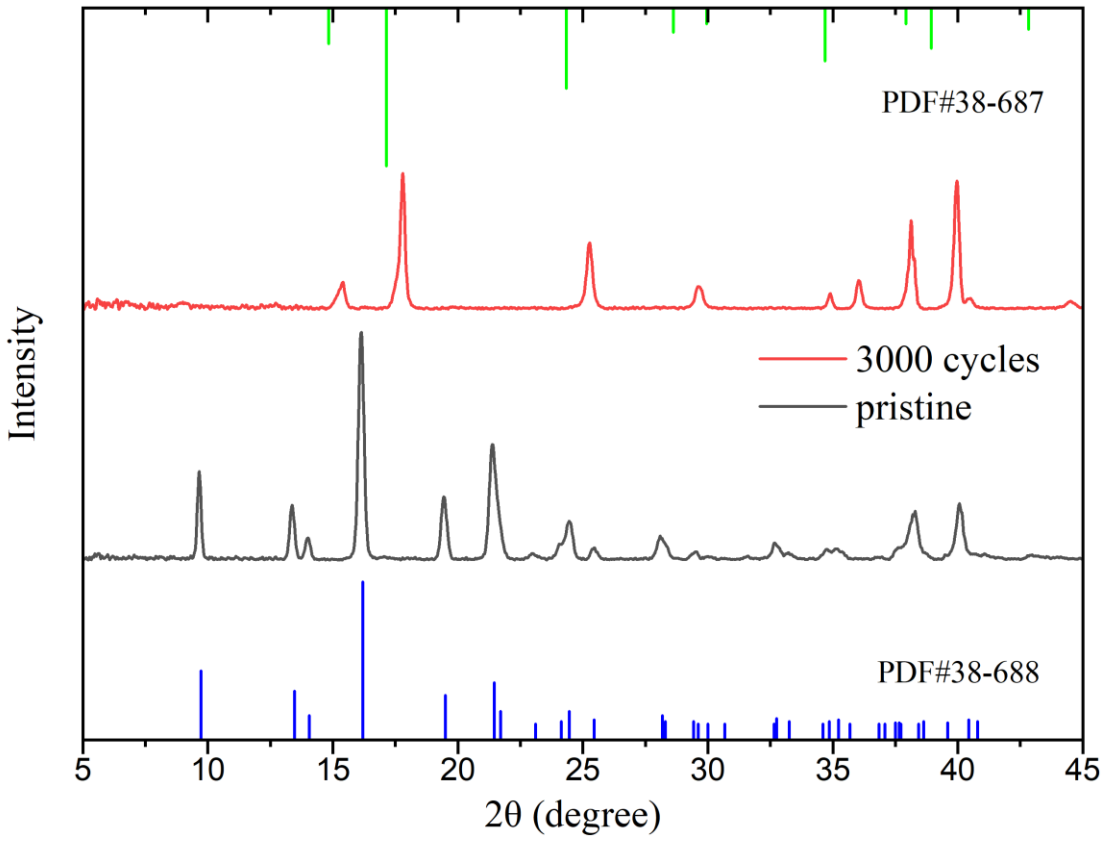

Fig. S4 XRD pattern of cathode material before and after 3000 cycles

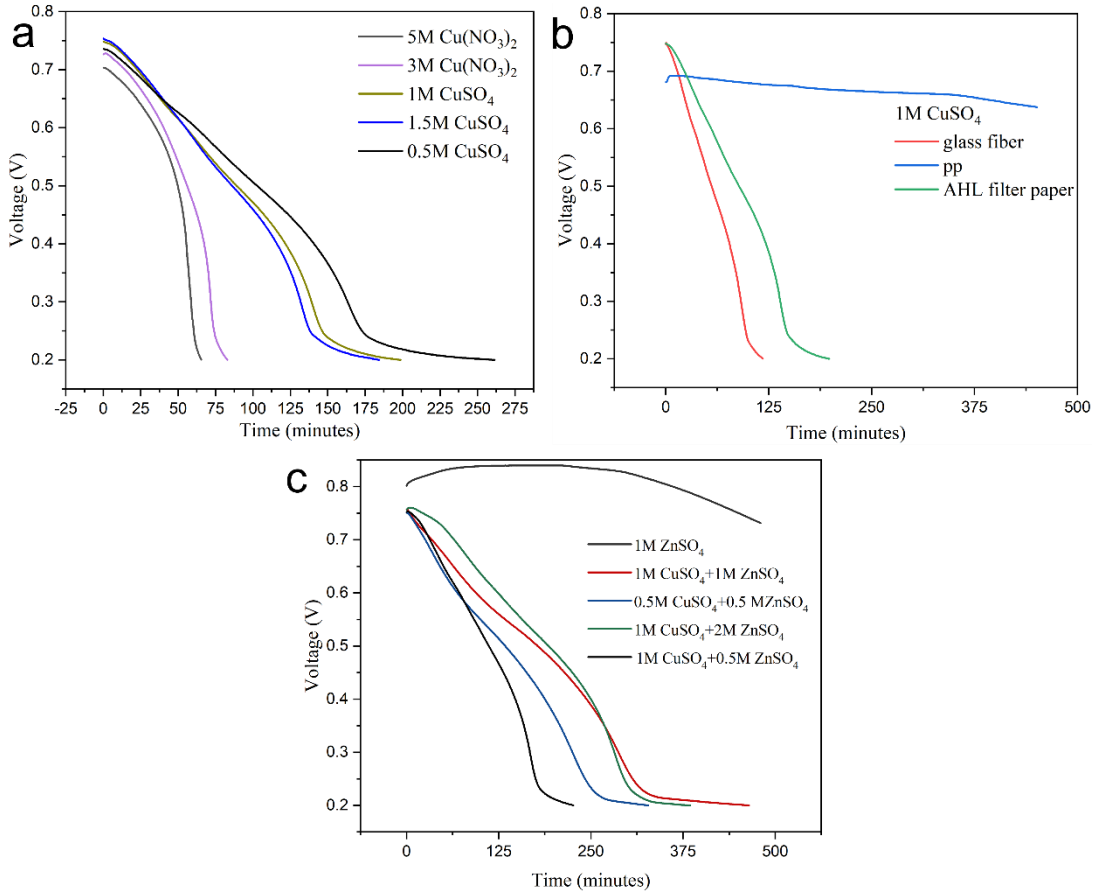

Fig. S5 open circuit voltage over time of (a) different copper ion concentrations (b) different separators (c) different concentrations of zinc ion

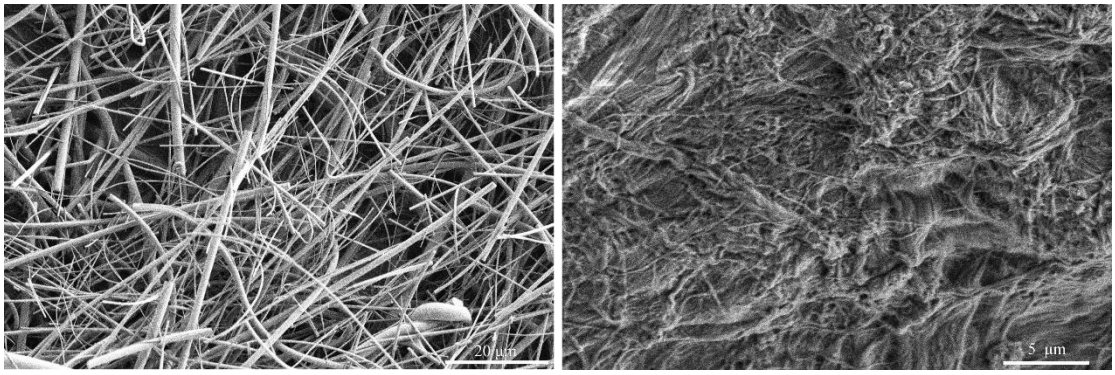

Fig. S6 SEM images of (left) Glass fiber separator and (right) AHL separator

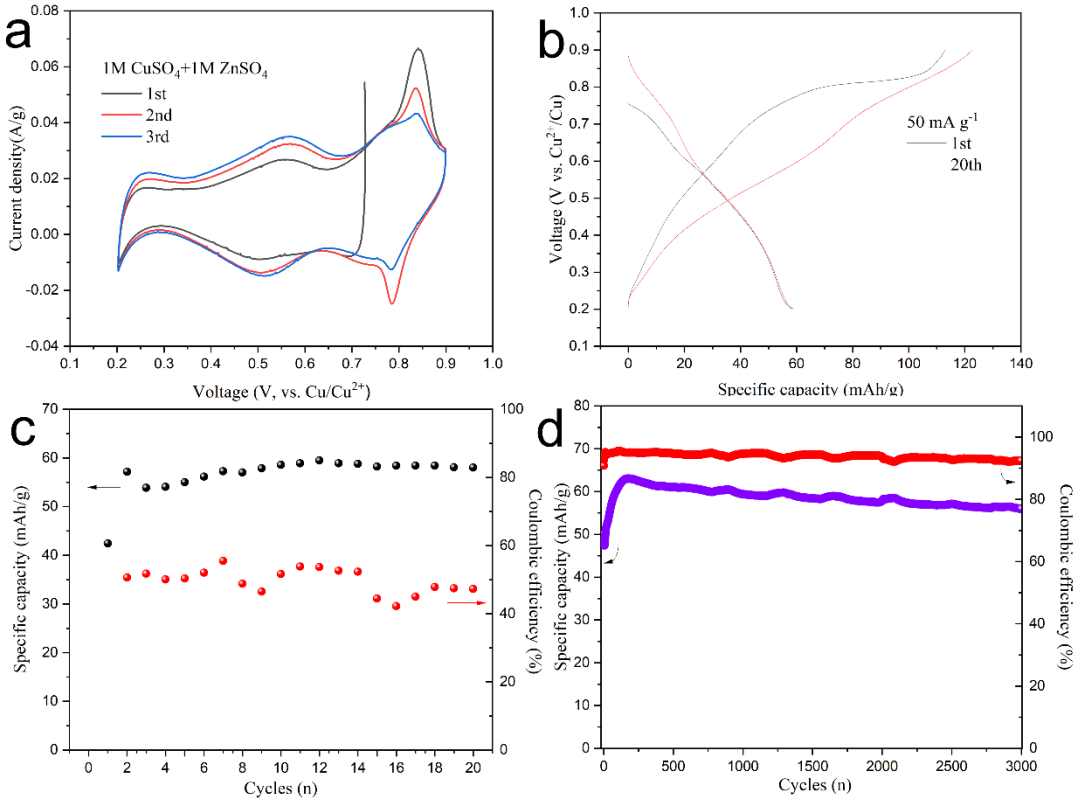

Fig. S7 CV curves of ZnHCF collected at a scan rate of 0.1 mV s^{-1}. (b) Voltage profiles of ZnHCF at 50 mA g^{-1}. (c) Cycling stability at 50 mA g^{-1}. (d) Cycling stability at 2 A g^{-1}.

Table 1

Concentration (mg/L)			Relative atomic ratio		
K	Zn	Fe	K	Zn	Fe
0.33	3.79	2.38	0.14	1.6	1

Table 2

Cathode	Anode	electrolyte	Specific capacity	Cycling performance	Ref.
ZnHCF	Zinc	1M $ZnSO_4$	65.4 mAh g^{-1} at a rate of 1 C	81% capacity retention after 100 cycles at 5 C	[1]
$Na_2Zn_3[Fe(CN)_6]_2 \cdot xH_2O$	Sodium	1M $NaClO_4$ in PC	56.4 mA h g^{-1} at 10 mA g^{-1}	85.2% capacity retention after 50 cycles at 10 mA g^{-1}	[2]

$K_{1.88}Zn_{2.88}[Fe(CN)_6]_2(H_2O)_5$	Potassium	0.5M KPF_6 in DEC& EC	55.6 mAh g^{-1} at 0.1 C	95% capacity retention after 100 cycles at 0.2 C	[3]
ZnHCF	Zinc	0.5M $ZnSO_4$ + 0.25M K_2SO_4	69.1 mAh g^{-1} at 2 C	74.1% capacity retention after 500 cycles at 20 C	[4]
$K_{0.11}Zn_{0.02}Mn[Fe(CN)_6]_{0.78}$	Lithium	1M $LiPF_6$ in DMC&EC with 5% FEC	519.3 mA h g^{-1} at 0.1 A g^{-1}	99.9% capacity retention after 5000 cycles at 1.0 A g^{-1}	[5]
ZnHCF	Sn doped In_2O_3	PAM polymer hydrogel electrolyte	75.3 mAh·g^{-1} at 0.4 A·g^{-1}		[6]

Reference:

[1] Zhang, L., Chen, L., Zhou, X., & Liu, Z. (2015). Towards high-voltage aqueous metal-ion batteries beyond 1.5 V: the zinc/zinc hexacyanoferrate system. Advanced Energy Materials, 5(2), 1400930.

[2] Lee, H., Kim, Y. I., Park, J. K., & Choi, J. W. (2012). Sodium zinc hexacyanoferrate with a well-defined open framework as a positive electrode for sodium ion batteries. Chemical Communications, 48(67), 8416-8418.

[3] Heo, J. W., Chae, M. S., Hyoung, J., & Hong, S. T. (2019). Rhombohedral potassium–zinc hexacyanoferrate as a cathode material for nonaqueous potassium-ion batteries. Inorganic chemistry, 58(5), 3065-3072.

[4] Huang, M., Meng, J., Huang, Z., Wang, X., & Mai, L. (2020). Ultrafast cation insertion-selected zinc hexacyanoferrate for 1.9 VK–Zn hybrid aqueous batteries. Journal of materials chemistry A, 8(14), 6631-6637.

[5] Fan, L., Guo, X., Hang, X., & Pang, H. (2022). Synthesis of truncated octahedral zinc-doped manganese hexacyanoferrates and low-temperature calcination activation for lithium-ion battery. Journal of Colloid and Interface Science, 607, 1898-1907.

[6] Wang, P., Wang, H., Chen, Z., Wu, J., Luo, J., & Huang, Y. (2022). Flexible aqueous Ca-ion full battery with super-flat discharge voltage plateau. Nano Research, 15(1), 701-708.